

# Weak lensing mass reconstruction using sparsity and a Gaussian random field

J.-L. Starck<sup>1</sup>, K. E. Themelis<sup>1</sup>, N. Jeffrey<sup>2,3</sup>, A. Peel<sup>4</sup>, and F. Lanusse<sup>1</sup>

<sup>1</sup> AIM, CEA, CNRS, Université Paris-Saclay, Université de Paris, F-91191 Gif-sur-Yvette, France

<sup>2</sup> Laboratoire de Physique de l'Ecole Normale Supérieure, ENS, Université PSL, CNRS, Sorbonne Université, Université de Paris, Paris, France

<sup>3</sup> Department of Physics & Astronomy, University College London, Gower Street, London, WC1E 6BT, UK


<sup>4</sup> Institute of Physics, Laboratory of Astrophysics, Ecole Polytechnique Fédérale de Lausanne (EPFL), Observatoire de Sauverny, 1290 Versoix, Switzerland

February 9, 2021

## ABSTRACT

**Aims.** We introduce a novel approach to reconstruct dark matter mass maps from weak gravitational lensing measurements. The cornerstone of the proposed method lies in a new modelling of the matter density field in the Universe as a mixture of two components: (1) a sparsity-based component that captures the non-Gaussian structure of the field, such as peaks or halos at different spatial scales; and (2) a Gaussian random field, which is known to well represent the linear characteristics of the field.

**Methods.** We propose an algorithm called MCALens which jointly estimates these two components. MCALens is based on an alternating minimization incorporating both sparse recovery and a proximal iterative Wiener filtering.

**Results.** Experimental results on simulated data show that the proposed method exhibits improved estimation accuracy compared to state-of-the-art mass map reconstruction methods. 

**Key words.** Cosmology: observations – Gravitational lensing: weak – Methods: numerical – Techniques: image processing

## 1. Introduction

In recent years, there has been increasing interest in exploring the two most dominant components of the universe, namely dark matter and dark energy. To this end, large-scale imaging and spectroscopic surveys are currently under development, such as the Euclid mission (Laureijs et al. 2011), the Rubin Observatory Legacy Survey of Space and Time (Abell et al. 2009), and the Roman Space Telescope (Spergel et al. 2015), that will map the sky with unprecedented accuracy. A prominent cosmological probe for these surveys is weak gravitational lensing.

Weak gravitational lensing measures correlations in the small distortions of distant galaxies caused by the gravitational potential of massive structures along the line of sight. Its impact on distant source galaxies is twofold: the galaxy shapes are magnified by a convergence field,  $\kappa$ , while the galaxies' ellipticities are perturbed from their underlying intrinsic value by a shear field,  $\gamma$ . To contribute constraints on cosmological parameters and models, two-point correlation functions of the shear have been utilised with considerable success (Kilbinger et al. 2013; Alsing et al. 2016b). This type of correlation is sufficient to statistically describe the Gaussian structures of the lensing field, such as those expected to be present either in the early universe or in large scales that are less affected by gravitational collapse. To capture non-Gaussian structures such as those expected in smaller scales at later time, higher order moments of the shear need to be employed (Munshi & Coles 2017).

On the other hand, the convergence density field is not observed directly as a result of the mass-sheet degeneracy (Bartelmann & Schneider 2001; Kilbinger 2015). Physically, the convergence field reveals the projected total matter density along the

line of sight, weighted by a lensing kernel in the mid-distance between the observer and the galaxy sources. The density field is inhomogeneous, encompassing Gaussian-type large-scale structures, as well as non-Gaussian features, such as peaks. To shed light on the way the convergence density field constrains cosmology, peak statistics (e.g. Jain & Van Waerbeke 2000; Marian et al. 2011; Lin & Kilbinger 2015; Liu & Haiman 2016; Peel et al. 2017b; Fluri et al. 2018; Li et al. 2019; Ajani et al. 2020) and higher order correlation functions and moments, such as the Minkowski functionals (e.g. Kratochvil et al. 2012; Shirasaki et al. 2012; Petri et al. 2013), have been applied directly on mass maps. It is therefore essential for mass mapping methods to preserve both Gaussian and non-Gaussian features during the reconstruction process.

Mass mapping methods solve an ill-posed problem due to the irregular sampling of the lensing field and the low signal-to-noise ratio on small scales. A widely used algorithm to perform mass mapping is the Kaiser-Squires method (Kaiser & Squires 1993), which is expressed as a simple linear operator in Fourier space. However, it is inevitable for this estimator to suffer from poor results, since it does not take special care of the noise or missing data. A different approach, motivated also by the Bayesian framework, is that of Wiener filtering (Wiener 1949). In this approach a Gaussian random field is assumed as a prior for the convergence map, which is responsible for inserting some bias that prevents our estimate from over-fitting (Zaroubi et al. 1995). Moreover, a recently proposed state-of-the-art method is the Gravitational Lensing Inversion and MaPping using Sparse Estimators (GLIMPSE2D) algorithm (Lanusse et al. 2016). GLIMPSE2D is a highly sophisticated algorithm that takes advantage of the sparse regularisation frame-

work to solve the ill-posed linear inverse problem. GLIMPSE2D is based on sparse representations (i.e. wavelets), and is therefore well designed to recover piece-wise smooth features. An analytical comparison between these three estimators is provided in Jeffrey et al. (2018a).

In this paper we propose to bridge the gap between the sparse regularisation method of GLIMPSE2D and the Wiener filtering method by modelling the matter density field in the universe using both linear and non-linear characteristics. Specifically, we assume that the density field is modelled as a mixture of two terms: (1) a non-Gaussian term that adopts a sparse representation in a selected wavelet basis (Starck et al. 2015), and (2) a Gaussian term that is modelled using a Gaussian random field (Elsner, F. & Wandelt, B. D. 2013; Horowitz et al. 2019). The non-Gaussian signal component is able to capture the non-linear characteristics of the convergence field, such as peaks, while the Gaussian component of the signal is responsible for capturing the lower-frequency characteristics of the underlying field, such as smooth variations. To our knowledge, this is the first time that this mixture modelling is proposed for mass map reconstruction.

This paper is structured as follows. In Sect. 2 we introduce the formalism of weak gravitational lensing and describe the mass map reconstruction problem. To this end, we provide a brief overview of the state-of-the-art algorithms of Kaiser-Squires, Wiener filtering, and GLIMPSE2D. We then present our proposed mass mapping method in Sect. 3. The method is novel in the sense that it exploits both sparsity in the wavelet domain as well as a Gaussian random field model. Section 4 illustrates the enhanced estimation performance of the proposed method by providing experiments conducted on both simulated and real data.

*Notation:* We use  $(\cdot)^*$  to denote the Hermitian transpose of a matrix or the adjoint operator of a transform. With  $\|\cdot\|_1$  and  $\|\cdot\|_2$  we denote the  $\ell_1$  and  $\ell_2$  norm respectively,  $(\|\mathbf{x}\|_1 = \sum_{i=1}^N |x_i|, \|\mathbf{x}\|_2^2 = \mathbf{x}^T \mathbf{x})$ . The determinant of a matrix or the absolute value of a scalar is denoted by  $|\cdot|$ , while  $\text{diag}(\mathbf{x})$  stands for a diagonal matrix, that contains the elements of vector  $\mathbf{x}$  on its diagonal. Finally,  $\mathcal{R}^N$  is the  $N$ -dimensional Euclidean space,  $\mathbf{0}$  denotes the zero vector,  $\mathbf{1}$  the all-ones vector, and  $\mathbf{I}_K$  is the  $K \times K$  identity matrix.

## 2. Weak lensing mass mapping

Gravitational lensing describes the phenomenon where the light emitted from distant galaxies is deflected as it passes through a foreground mass distribution. The lensing effect causes the images of distant galaxies to be distorted, with the distortion being proportional to the size and shape of the projected matter distribution along the line of sight. Specifically, the mapping between the source coordinates,  $\beta$ , and the lensed image coordinates,  $\theta$ , is given by the lens equation (e.g. Kilbinger 2015),

$$\beta = \theta - \nabla\psi(\theta), \quad (1)$$

where  $\psi(\cdot)$  defines the lensing potential that conceals the deflection of light rays by the gravitational lens. Under the Born approximation, which assumes that the lensing potential is *weak* enough, we may linearize the coordinate transformation of Eq. (1) by utilising the Jacobian  $\mathcal{A} = \partial\beta/\partial\theta$  as,

$$\beta_i = \mathcal{A}_{ij}\theta_j, \quad (2)$$

where  $\mathcal{A}_{ij} = \partial\beta_i/\partial\theta_j$  are the coefficients of the amplification matrix  $\mathcal{A}$ , and we assume the Einstein summation convention. The

symmetrical matrix  $\mathcal{A}$  can also be parameterised in terms of the *convergence*,  $\kappa$ , and the *shear*,  $\gamma$ , as,

$$\mathcal{A} = \begin{bmatrix} 1 - \kappa - \gamma_1 & -\gamma_2 \\ -\gamma_2 & 1 - \kappa + \gamma_1 \end{bmatrix}. \quad (3)$$

The convergence can then be defined as a dimensionless quantity that relates to the lensing potential through the Poisson equation,

$$\kappa = \frac{1}{2}(\partial_1\partial_1 + \partial_2\partial_2)\psi = \frac{1}{2}\nabla^2\psi, \quad (4)$$

while the shear is mathematically expressed as a complex field, whose components also relate to  $\psi$ ,

$$\gamma_1 = \frac{1}{2}(\partial_1\partial_1 - \partial_2\partial_2)\psi \text{ and } \gamma_2 = \partial_1\partial_2\psi. \quad (5)$$

From Eq. (3), we see that the convergence causes an isotropic change in the size of the source image, since it appears in the diagonal of  $\mathcal{A}$ . In comparison, the shear causes anisotropic changes to the image shapes. The convergence  $\kappa$  can also be interpreted via Eq. (4) as a weighted projection of the mass density field between the observation and the source. Factoring out the term  $(1 - \kappa)$  in Eq. (3) leaves the amplification matrix dependent on the reduced shear,

$$\mathcal{A} = (1 - \kappa) \begin{bmatrix} 1 - g_1 & -g_2 \\ -g_2 & 1 + g_1 \end{bmatrix}, \quad (6)$$

which is directly measured in lensing surveys and it is defined as  $g = \gamma/(1 - \kappa)$ . In the weak lensing limit, where  $\gamma, \kappa \ll 1$ , the reduced shear is approximately equal to the true shear, i.e.,  $g \simeq \gamma$ .

In this paper we are interested in recovering the convergence  $\kappa$  from the reduced shear data. This is an ill-posed inverse problem due to the finite sampling of the reduced shear over a limited area of the survey and the presence of shape noise in the measurements. In the following we review some of the state-of-the-art weak lensing mass reconstructing algorithms, namely the Kaiser-Squires, the Wiener filtering, and the GLIMPSE2D methods.

**Kaiser-Squires:** A theoretical framework for reconstructing convergence maps from the observable weak lensing shear in the Fourier domain was proposed in Kaiser & Squires (1993). As we have seen in Eqs. (4) and (5), the convergence and shear are both expressed as second order derivatives of the lensing potential. Their interrelation via the lensing potential  $\psi$  is expressed via a two-dimensional convolution (Kaiser & Squires 1993),

$$\gamma(\theta) = \frac{1}{\pi} \int_{\mathbb{R}^2} d^2\theta' \mathcal{D}(\theta - \theta') \kappa(\theta'), \quad (7)$$

where  $\mathcal{D}(\theta) = -1/(\theta_1 - i\theta_2)^2$ . This convolution is equivalently expressed in Fourier space as the element-wise multiplication,

$$\tilde{\gamma}(\mathbf{k}) = \pi^{-1} \tilde{\mathcal{D}}(\mathbf{k}) \tilde{\kappa}(\mathbf{k}), \quad (8)$$

where  $\mathbf{k}$  is the wavevector, and the Fourier transform of the kernel  $\mathcal{D}(\theta)$  is given by,

$$\tilde{\mathcal{D}}(\mathbf{k}) = \pi \frac{k_1^2 - k_2^2 + 2ik_1k_2}{k_1^2 + k_2^2}, \quad (9)$$

with  $k_1$  and  $k_2$  being the two frequency components of  $\mathbf{k}$ . Discretising Eq. 7 and adopting matrix notation, we may consider that the observed shear  $\gamma$  is generated as a linear combination of

the convolution matrix  $\mathbf{A}$  and the unknown underlying field  $\kappa$ , i.e.,

$$\gamma = \mathbf{A} \kappa + \mathbf{n}, \quad (10)$$

where  $\mathbf{n}$  is the statistical uncertainty vector associated with the data. Based on Eq. 8,  $\mathbf{A}$  can be decomposed in Fourier space as  $\mathbf{A} = \mathbf{F} \mathbf{P} \mathbf{F}^*$ , where  $\mathbf{F}$  denotes the discrete Fourier transform,  $\mathbf{F}^*$  is its adjoint, and  $\mathbf{P}$  is the diagonal operator that defines the convergence field-shear relation in Fourier space, namely

$$\tilde{\gamma} = \mathbf{P} \tilde{\kappa} = \left( \frac{k_1^2 - k_2^2}{k^2} + i \frac{2k_1 k_2}{k^2} \right) \tilde{\kappa} \quad (11)$$

where  $k^2 = k_1^2 + k_2^2$  and  $\tilde{\kappa} = \mathbf{F} \kappa$ .

Equation (11) corresponds to a discretised version of Eq. (8). As it stands, the Kaiser-Squires inversion of Eq. 11 suffers from several drawbacks. First, it is not defined for  $\mathbf{k} = 0$ , which stems from the mass-sheet degeneracy (i.e. the mean value of the convergence field cannot be retrieved). Next, it is ill-posed, because typically the shear field is a discrete under-sampling of the underlying convergence field. Also, it does not take into account masked data. Nonetheless, the Kaiser-Squires estimate is still used in practice due to its simplicity.

**Wiener filtering:** The Wiener filter was introduced in the 1940s (Wiener 1949), and it is the optimal linear filter in the minimum mean square sense that provides a denoised version of the desired signal. The Wiener filtered estimate of the convergence map can be expressed using the linear equation

$$\kappa_G = \mathbf{W} \gamma, \quad (12)$$

where the matrix  $\mathbf{W}$  is given by,

$$\mathbf{W} = (\mathbf{A} \Sigma_\kappa \mathbf{A}^* + \Sigma_n)^{-1} \mathbf{A}^* \Sigma_\kappa, \quad (13)$$

and  $\Sigma_\kappa$  and  $\Sigma_n$  are respectively the pre-defined covariance matrix of the convergence and the noise. When the noise is not stationary, the Wiener solution is not straightforward, and an iterative approach is required. This will be discussed in the next section.

From a Bayesian perspective, Wiener filtering is equivalent to the maximum a posteriori (MAP) estimator given that the convergence is a zero-mean Gaussian signal with covariance  $\Sigma_\kappa$ . Indeed, assuming that shear measurements are distorted by uncorrelated Gaussian noise, the likelihood function shares the noise properties, that is,

$$p(\gamma | \kappa, \Sigma_n) = |\pi \Sigma_n|^{-\frac{1}{2}} \exp \left[ -\frac{1}{2} (\gamma - \mathbf{A} \kappa)^* \Sigma_n^{-1} (\gamma - \mathbf{A} \kappa) \right], \quad (14)$$

while the distribution of the Gaussian random field can be written as

$$p(\kappa | \Sigma_\kappa) = |\pi \Sigma_\kappa|^{-\frac{1}{2}} \exp \left[ -\frac{1}{2} \kappa^* \Sigma_\kappa \kappa \right]. \quad (15)$$

Given Eqs. (14) and (15) above, the MAP estimator is expressed as

$$\begin{aligned} \kappa_G &= \arg \max_{\kappa} \{p(\kappa | \gamma)\} \propto \arg \max_{\kappa} \{p(\gamma | \kappa, \Sigma_n) p(\kappa | \Sigma_\kappa)\} \\ &\propto \arg \max_{\kappa} \exp \left[ -\frac{1}{2} \kappa^* \Sigma_\kappa \kappa - \frac{1}{2} (\gamma - \mathbf{A} \kappa)^* \Sigma_n^{-1} (\gamma - \mathbf{A} \kappa) \right], \end{aligned} \quad (16)$$

leading to minimize

$$\kappa_G = \arg \min_{\kappa} \left\{ \|\gamma - \mathbf{A} \kappa\|_{\Sigma_n}^2 + \|\kappa\|_{\Sigma_\kappa}^2 \right\}. \quad (17)$$

It is easy to see that the minimum is attained at  $\kappa_G = \mathbf{W} \gamma$ , where  $\mathbf{W}$  is the Wiener filter given in Eq. (12).

The implementation of the Wiener filter requires the inversion of the matrix  $\mathbf{W}$  that includes both a signal covariance matrix component and the noise covariance matrix component.

The unknown  $\kappa_G$  is assumed to be a Gaussian random field with a covariance matrix diagonal in Fourier space,  $\Sigma_\kappa = \mathbf{F}^* \mathbf{C}_\kappa \mathbf{F}$ , where  $\mathbf{C}_\kappa$  is a diagonal matrix with diagonal values equal to the theoretical power spectrum  $P_\kappa$ . When the noise is stationary, its covariance matrix is also diagonal with diagonal elements equal to the noise power spectrum  $P_n$ . In this case, the filter solution is obtained in Fourier space by  $\tilde{\kappa}_G = \tilde{\mathbf{W}} \tilde{\gamma}$ , where the Wiener filter is  $\tilde{\mathbf{W}} = \frac{P_\kappa}{P_\kappa + P_n}$ . In practice the noise is generally not stationary and depends on the number of shear measurements in the area related to a given pixel of the shear field. Therefore the noise covariance matrix is diagonal in pixel space, not in Fourier space, and the Wiener solution becomes more problematic to derive, requiring either making a wrong assumption (i.e. that the noise is stationary) or inverting a very large matrix. This renders its inversion computationally complex and prone to numerical errors. To circumvent this computationally intensive operation, a Forward-Backward (FB) proximal iterative Wiener filtering was proposed in Bobin et al. (2012) for Cosmic Microwave Background spherical map denoising, exploiting the property that the signal and noise covariance matrices are diagonal in pixel and Fourier space, respectively. Eq. (17) comprises two separable terms,

$$f_1(\kappa) = \|\gamma - \mathbf{A} \kappa\|_{\Sigma_n}^2 \text{ and } f_2(\kappa) = \|\kappa\|_{\Sigma_\kappa}^2. \quad (18)$$

Following Forward-Backward methodology (Starck et al. 2015), we can solve Eq. (18) by designing an iterative fixed point algorithm as

$$\kappa^{k+1} = \text{prox}_{\mu f_2}(\kappa_G^k + \nabla f_1(\kappa_G^k)), \quad (19)$$

which is known to converge when  $\mu < 2/\|\mathbf{A}^* \Sigma_n^{-1} \mathbf{A}\|_2$ , Combettes & Wajs (2005).

Computing the proximal operator in Eq. (19), we end up with the following iterative Wiener filtering algorithm,

– Forward step:

$$\mathbf{t} = \kappa^n + 2\mu \mathbf{A}^* \Sigma_n^{-1} (\gamma - \mathbf{A} \kappa^n) \quad (20)$$

– Backward step:

$$\kappa^{n+1} = \mathbf{F}^* \left( \mathbf{P}_\kappa (\mathbf{P}_\eta + \mathbf{P}_\kappa)^{-1} \right) \mathbf{F} \mathbf{t}, \quad (21)$$

where  $\mathbf{t}$  is an auxiliary variable,  $\mu = \min(\Sigma_n)$ ,  $\mathbf{P}_\eta = 2\mu \mathbf{I}$  and  $\kappa^0 = 0$ . This algorithm is free from matrix inversions, since both  $\Sigma_n$  used in Eq. (20) and  $\mathbf{P}_\kappa$  used in Eq. (21) are diagonal matrices. A similar algorithm, exploiting transformations between pixel and harmonic space, was proposed by Elsner, F. & Wandelt, B. D. (2013) using the messenger field framework. Such methods can also be adapted to efficiently sample from the posterior distribution of the unknown mass map (Alsing et al. 2017; Jeffrey et al. 2018b). The Wiener approach recovers the Gaussian component of the convergence field well, but it is far from optimal at extracting the non-Gaussian information from the data, as peak-like structures are suppressed. This has motivated the development of sparse recovery methods based on wavelets.

**Sparse Recovery:** It has been shown that sparse recovery using wavelets is a very efficient way to reconstruct convergence maps (Starck et al. 2006; Leonard et al. 2012; Lanusse et al.

2016; Peel et al. 2017a; Price et al. 2020a). The mass mapping problem is addressed as a general ill-posed problem, which is solved via weighted  $\ell_1$ -norm regularization in a wavelet-based analysis sparsity model. Sparsity in the Discrete Cosine Transform (DCT) domain was also proposed to fill the missing data area in the convergence map (Pires et al. 2009).

The GLIMPSE algorithm avoids any binning or smoothing of the input data that could potentially cause loss of information. The primary cost function is

$$\arg \min_{\kappa} \left\{ \frac{1}{2} \|\gamma - \mathcal{T} \mathbf{P} \mathcal{F}^* \kappa\|_{\Sigma_n}^2 + \lambda \|\omega \odot \Phi^* \kappa\|_1 + i_{\mathbb{R}}(\kappa) \right\} \quad (22)$$

where  $\mathcal{T}$  is the nonuniform discrete Fourier transform (NDFT) matrix,  $\mathbf{P}$  is defined in Eq. (11),  $\lambda$  is a sparsity regularization parameter,  $\omega$  is a weighting vector,  $\Phi^*$  is the adjoint operator of the wavelet transform, and  $i_{\mathbb{R}}$  is an identity function that drives the imaginary part of the convergence to zero. This cost function is also generalised in GLIMPSE2D in order to replace the shear by the reduced shear, or to incorporate the flexion information. It has been shown that GLIMPSE2D significantly outperforms Wiener filtering for peaks recovery, while Wiener filtering does better on the Gaussian map content (Jeffrey et al. 2018a).

*Deep Learning:* Deep learning techniques have recently been proposed and seem very promising (Jeffrey et al. 2020). The input of the neural network is not the shear field directly, but rather the Wiener solution. We could imagine that the closer we are to the true solution with standard techniques such as Wiener or sparsity, the better deep learning can improve the solution. Open questions related to deep learning remain to be answered, such as its generalization to cosmologies not present in the training data set, or the potential bias introduced by using a theoretical power spectrum in the Wiener solution serving as input of the neural network.

### 3. Modelling with sparsity and a Gaussian random field

#### 3.1. A new convergence map model

We have seen in Sect. 2 two different models: the first modelling the convergence map as a Gaussian random field, leading to good recovery of the large scales of the convergence map but suppression peak structures, and the second assuming the convergence map is compressible in the wavelet domain (i.e. sparse modelling). The sparse recovery is clearly complementary to the Wiener solution, since it recovers peaks extremely well but the Gaussian content poorly.

To address these limitations, it seems natural to introduce a novel modelling approach, where the convergence field  $\kappa$  is assumed to comprise two parts, a Gaussian and a non-Gaussian:

$$\kappa = \kappa_G + \kappa_{NG}. \quad (23)$$

The non-Gaussian part of the signal  $\kappa_{NG}$  is subject to a sparse decomposition in a wavelet dictionary, while the component  $\kappa_G$  is assumed to be inherently non-sparse and Gaussian.

The Morphological Component Analysis (MCA) was proposed in Starck et al. (2004); Elad et al. (2005) to separate two components mixed in a single image when these components have different morphological properties. This looks impossible, since we have two unknowns and one equation, but it was shown that it is sometimes possible to extract these two components if we can exploit their morphological differences. This requires

having different penalisation functions  $C_G$  and  $C_{NG}$  on each of these two components, and we need to minimise

$$\min_{\kappa_G, \kappa_{NG}} \left\{ \|\gamma - \mathbf{A}(\kappa_G + \kappa_{NG})\|_{\Sigma_n}^2 + C_G(\kappa_G) + C_{NG}(\kappa_{NG}) \right\}. \quad (24)$$

MCA performs an alternating minimization scheme:

- Estimate  $\kappa_G$  assuming  $\kappa_{NG}$  is known:

$$\min_{\kappa_G} \left\{ \|\gamma - \mathbf{A} \kappa_{NG} - \mathbf{A} \kappa_G\|_{\Sigma_n}^2 + C_G(\kappa_G) \right\}. \quad (25)$$

- Estimate  $\kappa_{NG}$  assuming  $\kappa_G$  is known:

$$\min_{\kappa_{NG}} \left\{ \|\gamma - \mathbf{A} \kappa_G - \mathbf{A} \kappa_{NG}\|_{\Sigma_n}^2 + C_{NG}(\kappa_{NG}) \right\}. \quad (26)$$

Examples of such decompositions can be seen on the MCA web page<sup>1</sup>. A range of MCA applications in astrophysics can be found in Starck et al. (2003); André et al. (2010); Möller et al. (2015); Bobin et al. (2016); Melchior et al. (2018); Joseph et al. (2019); Wagner-Carena et al. (2020).

#### The Gaussian component $\kappa_G$

We use here the standard Wiener modeling where  $\kappa_G$  is assumed to be a Gaussian random field:

$$C_G(\kappa_G) = \|\kappa\|_{\Sigma_n}^2, \quad (27)$$

and the solution of Eq. (25) is obtained using the iterative Wiener filtering presented in the previous section.

#### The non-Gaussian component

There are different ways to use a sparse model in the MCA framework. The most obvious would be to use standard  $\ell_1$  or  $\ell_0$ -norm regularisation in a wavelet-based sparsity model, as it is done in the GLIMPSE2D algorithm. This would give:

$$C_{NG}(\kappa_{NG}) = \lambda \|\Phi^* \kappa_{NG}\|_p, \quad (28)$$

where  $p = 0$  or  $1$ ,  $\Phi$  is the wavelet matrix, and  $\lambda$  is the regularization parameter (Lagrange multiplier).

After implementing this approach, we found that large wavelet scales and Fourier low frequencies are relatively close, leading to difficulties in separating the information. We have therefore investigated another approach, which involves first estimating the set  $\Omega$  of active coefficients—i.e. the scales and positions where wavelet coefficients are above a given threshold—typically between 3 and 5 times the noise standard deviation relative to each wavelet coefficient.  $\Omega$  can therefore be seen as a mask in the wavelet domain, where  $\Omega_{j,x} = 1$  if a wavelet coefficient detected at scale  $j$  and position  $x$ , i.e. when  $|\Phi^* \mathbf{A}^* \gamma|_{j,x} > \lambda \sigma_{j,x}$ , and 0 otherwise. The noise  $\sigma_{j,x}$  at scale  $j$  and position  $x$  can be determined using noise realizations as in the GLIMPSE algorithm. An even faster approach is to detect the significant wavelet coefficients on  $\Phi^* \mathbf{A}^* \Sigma_n^{-1/2} \gamma$  instead of  $\Phi^* \mathbf{A}^* \gamma$ . The noise is therefore whitened, as the noise factor  $\mathbf{A}^* \Sigma_n^{-1/2}$  is Gaussian with standard deviation equal to unity and with a uniform power spectrum. We implemented both approaches giving similar results, though the second is simpler.

Once this wavelet mask  $\Omega$  is estimated, we can estimate the non Gaussian component  $\kappa_{NG}$  by

$$\min_{\kappa_{NG}} \left\{ \|\Omega \odot \Phi^* ((\gamma - \mathbf{A} \kappa_G) - \mathbf{A} \kappa_{NG})\|_{\Sigma_n}^2 + C_{NG}(\kappa_{NG}) \right\}. \quad (29)$$

<sup>1</sup> <http://jstarck.cosmostat.org/mca>

with  $C_{NG}(\kappa_{NG}) = \hat{\mathbb{I}}_{\mathbb{R}}(\kappa_{NG})$ .

This changes the original formalism since the data fidelity term is now different, but it presents a very interesting advantage. Once  $\Omega$  is fixed, the algorithm is almost linear and only the positivity constraint remains. Therefore, we can easily derive a good approximation of the error map, just by propagating noise and relaxing this positivity constraint. This will be further discussed in the following. Similarly to the GLIMPSE method, a positivity constraint is applied on the non-Gaussian component  $\kappa_{NG}$ . Peaks in  $\kappa$  can be on top of voids, and therefore have negative pixel values. As peaks are captured by the non-Gaussian component, they are positive by construction in  $\kappa_{NG}$ , but the convergence map  $\kappa = \kappa_G + \kappa_{NG}$  can still be negative at peaks positions. Larger are the non-Gaussianities, more we can expect MCAIens to improve over linear methods such as the Wiener one.

The prior signal auto-correlation of the Gaussian component is included within the signal covariance term of the Gaussian component. We encode no explicit prior auto-correlation for the non-Gaussian signal and no explicit prior cross-correlation between the Gaussian and non-Gaussian component. Clearly, such correlations exist but including their contribution in the prior in this framework would be extremely difficult theoretically and in practice. However, such correlations will still appear in the final reconstruction, driven by the correlation information in the data.

### 3.2. MCAIens Algorithm

---

#### Algorithm 1 MCAIens algorithm

---

- 1: **Input:** Shear map  $\gamma_1, \gamma_2$ , signal and noise covariance  $\Sigma_\kappa, \Sigma_n$ , and detection level  $\lambda$ .
  - 2: Initialize:  $\kappa_{NG}^{(0)} = \kappa_G^{(0)} = \Omega = 0, \mu = \min(\Sigma_n), \mathbf{P}_\eta = 2\mu\mathbf{I}$ .
  - 3: Calculate wavelet coefficients:  $\alpha = \Phi^* \mathbf{A}^* \Sigma_n^{-\frac{1}{2}} \gamma$ .
  - 4:  $\forall j, x$ , set  $\Omega_{j,x} = 1$  if  $|\alpha|_{j,x} > \lambda$ .
  - 5: **for**  $n = 0, \dots, N_{\max} - 1$  **do**
  - 6:     Find  $\kappa_{NG}$
  - 7:     Calculate the shear residual:  $\gamma_r = \gamma - \mathbf{A}(\kappa_G^{(n)} + \kappa_{NG}^{(n)})$ .
  - 8:     Calculate the sparse residual:  $s_r = \mathbf{A}^* \Sigma_n^{-\frac{1}{2}} \gamma_r$ .
  - 9:     Calculate the sparse residual in the mask:  
 $s_{mr} = \Phi(\Omega \odot (\Phi^* s_r))$ .
  - 10:    Get the new sparse component:  $\mathbf{S} = \kappa_{NG}^{(n)} + s_{mr}$ .
  - 11:    Positivity constraint:  $\kappa_{NG}^{(n+1)} = [\mathbf{S}]_+$ .
  - 12:    Find  $\kappa_G$
  - 13:    Calculate the shear residual:  $\gamma_r = \gamma - \mathbf{A}(\kappa_G^{(n)} + \kappa_{NG}^{(n+1)})$ .
  - 14:    Forward step:  $\mathbf{t} = \kappa_G^{(n)} + 2\mu \mathbf{A}^* \Sigma_n^{-1} \gamma_r$ .
  - 15:    Backward step:  $\kappa_G^{n+1} = \mathbf{F}^* \left( \mathbf{P}_\kappa (\mathbf{P}_\eta + \mathbf{P}_\kappa)^{-1} \right) \mathbf{F} \mathbf{t}$ .
  - 16: **end for**
  - 17: **return**  $(\kappa_G^{(N_{\max})}, \kappa_{NG}^{(N_{\max})})$ .
- 

We solve the recovery problem of Eq. (23) using a two-step optimization procedure. First, a gradient descent step to minimise Eq. (29) to recover the non-Gaussian component  $\kappa_{NG}$ . This is followed by an iteration of the iterative Wiener filtering to minimise Eq. (17). Details of the method are given in the Algo. 1.

The number of scales  $N_s$  used to compute the wavelet transform of an  $N_x \times N_y$  image is automatically derived by  $N_s = \text{int}(\log(\min(N_x, N_y)))$ . The  $\lambda$  parameter is a detection level, which was fixed for all our experiments with real and simulated data to 5, i.e. 5 times the noise standard deviation, which is a conservative threshold which gave excellent results.

### 3.3. Errors

Much attention has recently been given to the estimation of errors or uncertainties with mass map products. For linear methods such as Wiener or Kaiser-Squires, it is easy to estimate the standard deviation (or root-mean-square, RMS) per pixel, just by propagating noise realisations using the same reconstruction filters. The uncertainty per pixel does not, however, give the probability that a clump in a reconstructed image is true or only due to some noise fluctuations. Another approach, closer to certain science cases with maps, estimates the significance of clumps. In Peel et al. (2017a), Monte Carlo simulations were used to address the significance of clumps. In Repetti et al. (2019), a hypothesis test called BUQO was proposed to do the same task, requiring the user to define manually a mask around the clump. Similarly, in Price et al. (2019), hypothesis tests of Abell-520 cluster structures using Highest Posterior Density Regions were performed.

With MCAIens, we can include aspects of both approaches.

### RMS and SNR maps

In Algo. 1, there are two steps involving a non-linear operator, first for the estimation of  $\Omega$  in line 4 and the second in line 11 to perform the positivity constraint. To propagate noise realizations,  $\Omega$  has to be set to the one obtained with the data, and this non-linearity step therefore does not occur, so only the positivity remains. A full linear algorithm could therefore be obtained just by removing this positivity constraint during the noise propagation, by replacing  $\kappa_{NG}^{(n+1)} = [\mathbf{S}]_+$  in Algo. 1 line 11 by  $\kappa_{NG}^{(n+1)} = \mathbf{S}$ . This leads to more noise entering the solution, since few pixel values with negative values in  $\kappa_{NG}$  are not thresholded, and the derived RMS map is therefore slightly conservative. Hence, we can build noise realizations, run the MCAIens algorithm on each realization, and derive the RMS map by taking pixel per pixel the standard deviation of the obtained reconstructed maps. The SNR map is derived by dividing the absolute value of the reconstructed map by the RMS map.

### Significance map

In Algo. 1 line 4, the wavelet mask  $\Omega$  is obtained by comparing the wavelet coefficients,  $\alpha = \Phi^* \mathbf{A}^* \Sigma_n^{-\frac{1}{2}} \gamma$ , to the threshold  $\lambda\sigma$  where  $\sigma = 1$  as the noise is whitened with unit variance. This corresponds to performing a hypothesis test  $H_0$  that the wavelet coefficient is due to noise only, and if a given wavelet coefficient  $\alpha_{j,x}$  is such that  $|\alpha_{j,x}| > \lambda$ , then the  $H_0$  hypothesis is rejected and we assume that the coefficient amplitude cannot be explained by noise fluctuations and is therefore due to signal.  $\lambda$  is therefore directly related to the significance of the wavelet coefficients, and the mask  $\Omega$  indicates which coefficients are detected with a given significance level.  $\Omega_{j,x}$  is binary, and we build the significance map  $s$  by  $s_x = \sum_j \Omega_{j,x}$ , i.e. a simple coadding of all binary scales. Such a map could also be used as a way to automatically derive the user mask required in the BUQO method (Repetti et al. 2019). We present in Sect. 4 examples of RMS, SNR and significance maps.

### 3.4. Extension to the Sphere

When a wide-field map needs to be reconstructed, the flat approximation cannot be used anymore, and we have to build a map on the sphere. A traditional approach is to decompose the

sphere into overlapping patches, assume a flat approximation on each individual patch, reconstruct each patch independently, and finally recombine all patches on the sphere. This solution is certainly good enough to recover clumps relative to clusters, i.e. the non-Gaussian component, but certainly not for the Gaussian component which contains information at low frequencies. In the framework of the DES project, a 1500 deg<sup>2</sup> map has been reconstructed Chang et al. (2018), using HEALPIX pixelisation (Górski et al. 2005) and a straightforward spherical Kaiser-Squires algorithm consisting in:

1. calculating a spin transform of the HEALPIX shear map to get both the E and B spherical harmonic coefficients,
2. smoothing by a Gaussian both E and B modes in the spherical harmonic domain,
3. applying an inverse spherical transform independently on each of these two modes to get the two convergence maps  $\kappa^E$  and  $\kappa^B$ .

Sparsity in a Bayesian framework (Price et al. 2020b) and forward fitting in harmonic space (Mawdsley et al. 2020) have also been recently proposed to do spherical mass mapping. Using similarly a HEALPIX shear and convergence pixelisation, we can also easily derive an extension of both the iterative-Wiener filtering and the MCAIens algorithm by

- replacing the matrix  $\mathbf{A} = \mathbf{F}\mathbf{P}\mathbf{F}^*$  in Eq. (10) by  $\mathbf{A} = \mathbf{2}\mathbf{Y}_0\mathbf{Y}^*$ , where  $\mathbf{Y}$  and  $\mathbf{Y}^*$  represent the forward and inverse spin-s spherical harmonic transforms respectively,
- replacing the wavelet decomposition  $\Phi$  used in Eq. (28) by the spherical wavelet decomposition (Starck et al. 2006).

Then the same MCAIens algorithm given in Algo. 1 can be used to derive a spherical convergence map. An example is given in Sect. 4.3.

### 3.5. B-mode

We focused earlier on the convergence map (i.e. E-mode). The MCAIens algorithm given in Algo. 1 remains valid if one wants to estimate both E and B mode by adopting the following notation:

$$\gamma = \begin{pmatrix} \gamma_1 \\ \gamma_2 \end{pmatrix}, \kappa = \begin{pmatrix} \kappa_E \\ \kappa_B \end{pmatrix}, \mathbf{A} = \begin{pmatrix} \frac{k_1^2 - k_2^2}{k^2} & \frac{2k_1 k_2}{k^2} \\ \frac{2k_1 k_2}{k^2} & -\frac{k_1^2 - k_2^2}{k^2} \end{pmatrix}, \alpha = \begin{pmatrix} \alpha_E \\ \alpha_B \end{pmatrix}, \mathbf{P}_\kappa = \begin{pmatrix} \mathbf{P}_{\kappa_E} \\ \mathbf{P}_{\kappa_B} \end{pmatrix}, \Phi = \begin{pmatrix} \Phi_E \\ \Phi_B \end{pmatrix},$$

where the matrix  $\Phi$  consists in applying a sparse decomposition independently on each mode. In practice we use the same wavelet decomposition for both (i.e.  $\Phi_E = \Phi_B$ ). The delicate point is the Wiener filter to apply to the B-mode at line 15 of the algorithm. In theory,  $\mathbf{P}_{\kappa_B} = 0$ , and by construction, no Gaussian component can be recovered. Since the B-mode is mainly useful for investigation of systematic errors, we are not interested in recovering the B-mode least square estimator (which is zero), and we find it more useful to process the B-mode similarly to the E-mode. We therefore advocate rather to use  $\mathbf{P}_{\kappa_B} = \mathbf{P}_{\kappa_E}$ . This way the fluctuations in the E-mode can properly be compared to those in the B-mode.

## 4. Experimental results

### 4.1. Toy Model Experiment

We use a simulation derived from RAMSES N-body cosmological simulations (Teyssier 2002), with a  $\Lambda$ CDM model (see

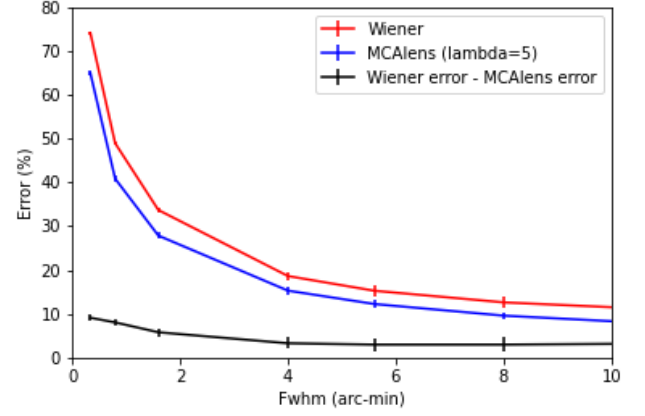


**Fig. 1.** RAMSES simulations: Error versus scale for Wiener in red and MCAIens in blue.

<http://www.projet-horizon.fr>), with a pixel size of 0.34' x 0.34' and a galaxy redshift of 1. To get a realistic mask and noise behavior, we use the MICE pixel noise covariance derived for the DES project (see Appendix A). As the pixel resolution is different, it leads to an optimistic realization, but it has the advantage of illustrating well the impact of our MCA model.

We have run MCAIens using 100 iterations,  $\lambda = 5$  (i.e. detection at  $5\sigma$ ), the MICE covariance matrix, and the used theoretical power spectrum was the true map power spectrum. To evaluate the results, we ran 100 different noise realizations, and we applied both Wiener filtering and MCAIens. We calculated the reconstruction error at different resolutions with

$$Err_{\%}(\sigma) = \frac{\| \mathbf{G}_{\sigma}(\mathbf{M}(\kappa - \kappa_t)) \|}{\| \mathbf{M}\kappa_t \|} \quad (30)$$

where  $\|x\| = \sqrt{\sum_i x_i^2}$ ,  $\kappa$  is the reconstruct convergence map,  $\kappa_t$  the true convergence map,  $\mathbf{G}_{\sigma}(x)$  is the convolution of  $x$  with a Gaussian with standard deviation  $\sigma$ , and  $\mathbf{M}$  is the binary mask with  $M_k = 1$  if the covariance matrix is not infinite at location  $k$  (i.e. we have data at this location) and 0 otherwise. Figure 1 shows the mean error  $Err_{\%}(\sigma)$  for both the Wiener and MCAIens solutions. The black curve shows the difference between the Wiener error and the MCAIens error, allowing to better visualise that the improvement is larger at fine scales. It is interesting to note that at MCAIens is better than Wiener even at large scales. Indeed, when the MCAIens non-Gaussian component contains a significant amount of features as in the case of this experiment, these features have also a non negligible contribution on larger scales, which explain why MCAIens remains better than Wiener at large scales. MCAIens leads to a clear improvement in terms of quadratic error. The top panels of Fig. 2 show respectively the simulated convergence map and the MCAIens reconstructed map. The bottoms panels show the Gaussian and the non Gaussian part recovered from the noisy the data. The sum of these two components is equal to the MCAIens reconstruction (top right). This shows that both the non-linear and the linear components can be recovered well. Figure 3 shows respectively the RMS map, the SNR map and the significance map.

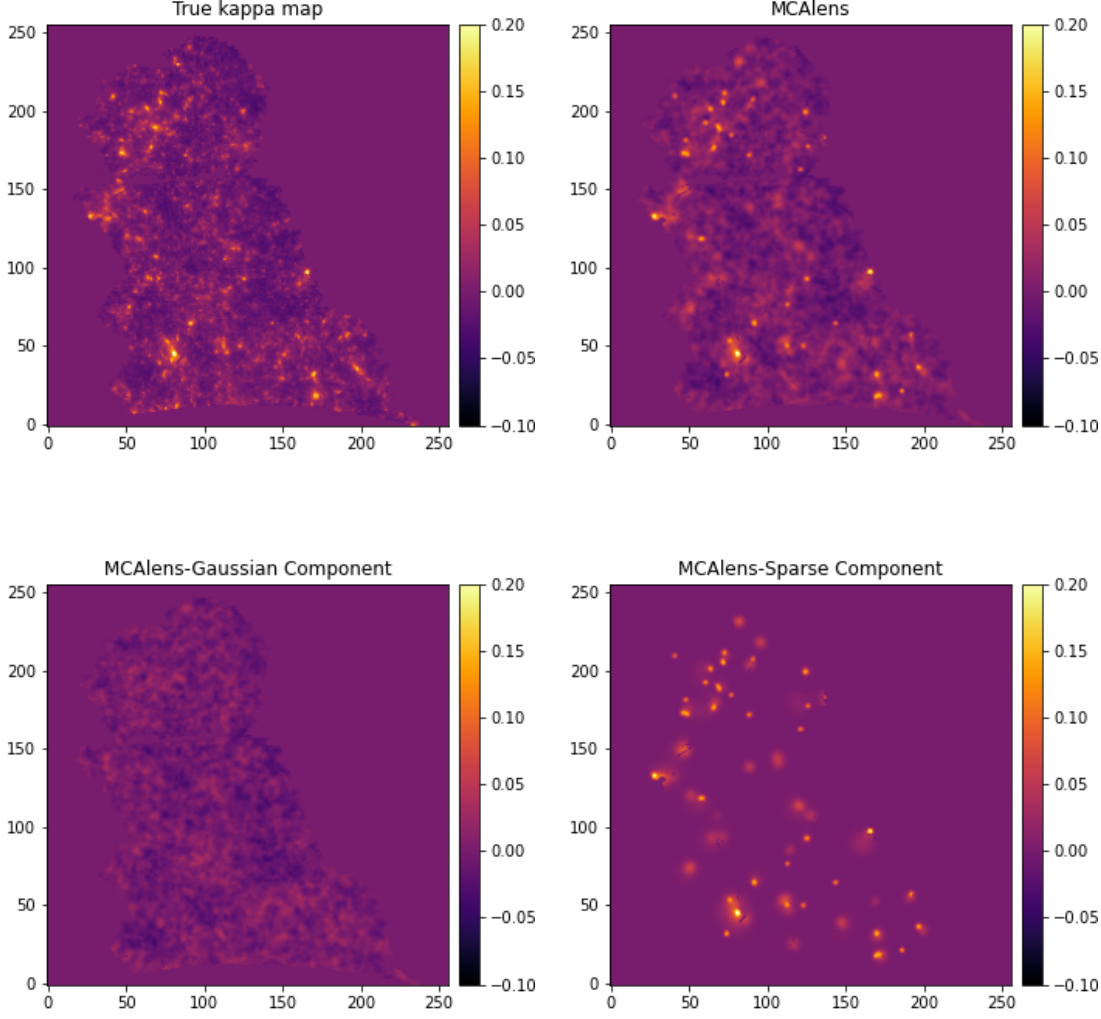


**Fig. 2.** RAMSES simulations: Top, true convergence map and MCAIens recovery; bottom, Gaussian components and sparse components. The sum of these two maps is equal to the top right MCAIens map.

#### 4.2. Columbia Lensing Simulation

We use here a convergence map, released by the Columbia Lensing group<sup>2</sup> (Liu et al. 2018), corresponding to a cosmological model with parameters  $\{M_v, \Omega_m, 10^9 A_s, M_v, h, w\} = \{0.1, 0.3, 2.1, 0, 0.7, -1\}$ , and with a pixel size of  $0.4' \times 0.4'$ . We rebinned the map to  $0.8' \times 0.8'$ , and similarly to the previous experiment, we simulated noisy data using the same MICE covariance, applying a global rescaling in order to have realistic noise corresponding to a mean number of galaxies equal to 30 per  $\text{arcmin}^2$ , as we expect in future space lensing surveys. To evaluate the results, we ran 100 different noise realizations, and we applied Kaiser-Squires, sparse recovery, Wiener filtering, and MCAIens. For the sparse recovery and MCAIens, we used  $\lambda = 5$  (i.e. detection at  $5\sigma$ ), and for Wiener and MCAIens we used the theoretical power spectrum as the true convergence map power spectrum.

Figure 4 shows the error computed using Eq. (30). We can see that, in addition to the well-recovered peaks, MCAIens also leads to a clear improvement in terms of quadratic er-

ror compared the other methods. On the contrary to the RAMSES experiment, we see here a convergence at large scales between MCAIens and Wiener. This is due that the MCAIens non-Gaussian component contains only a few peaks (see Fig. 5, middle right), which have therefore a negligible contribution to the largest scales.

The top row of Fig. 5 shows respectively the simulated convergence map, the Wiener result, and the Kaiser-Squires reconstruction with smoothing applied. The middle shows the MCAIens map and its Gaussian and non Gaussian parts recovered from the noisy the data. The sum of these two components is equal to the MCAIens. Similarly to previous experiments, both the non-linear and the linear components are well recovered. The bottom row of Fig. 5 shows respectively the RMS map, the SNR map and the significance map.

#### 4.3. Spherical Data

We have created a full shear map from the full sky MICE simulated map and its covariance matrix, which has around 3 galaxies per  $\text{arcmin}^2$ . We ran the spherical MCAIens method with 200 it-

<sup>2</sup> <http://columbialensing.org>



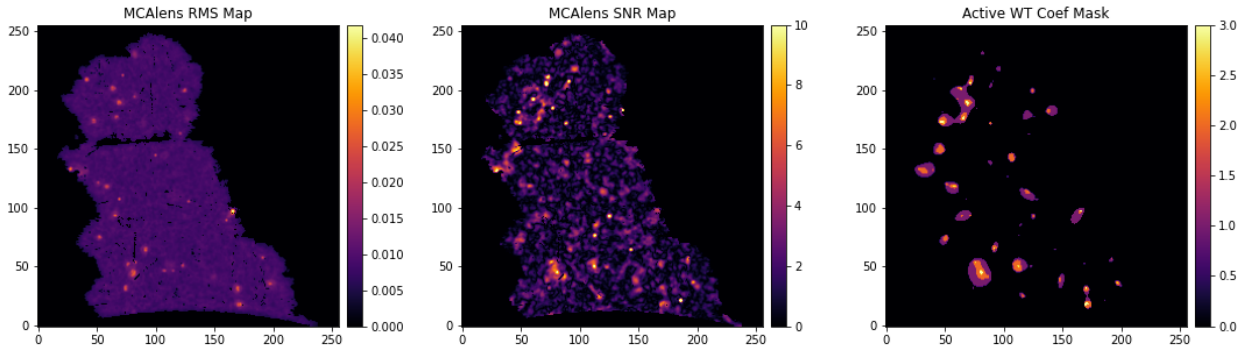


**Fig. 3.** RAMSES simulations: from left to right, RMS map, SNR map and significance map.

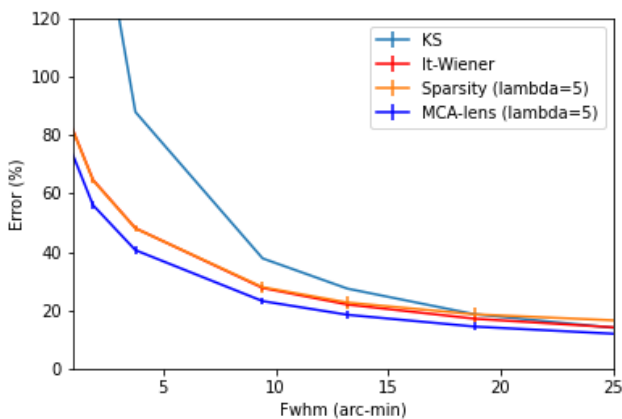


**Fig. 4.** Columbia simulations: error versus scale for four different methods: Kaiser-Squires (light blue), Wiener (red), sparsity (orange) and MCA lens (blue).

erations,  $\lambda = 5$  (i.e. detection at  $5\sigma$ ), and we used the power spectrum of the simulation as the theoretical power spectrum. The top row of Fig. 6 shows the simulated noise-free map at 1 and 3 degrees, while the bottom row shows the MCA lens non-Gaussian and Gaussian components.

#### 4.4. COSMOS field

In this last section, we apply MCA lens to reconstruct a convergence map of the  $1.64 \text{ deg}^2$  HST/ACS COSMOS survey (Scoville et al. 2007). In this work, we make use of the bright galaxies shape catalogue produced for (Schrabback et al. 2010).

The results after applying MCA lens on COSMOS data are presented in Fig. 7. In the top row are the galaxy count map, the Wiener map, and the Kaiser-Squires map smoothed with a Gaussian at a Full Width at Half Maximum of 2.4 arcmin. The bottom row shows respectively the Glimpse, MCA lens E-mode and MCA lens B-mode maps. White dots show the locations and redshifts of X-ray selected massive galaxy clusters from the XMM-Newton Wide Field Survey (Finoguenov et al. 2007) with  $0.3 < z < 1.0$ .

## 5. Conclusion

A novel mass mapping algorithm has been presented that is able to recover high resolution convergence maps from weak gravitational lensing measurements. Our proposed process involves a model with two components, a Gaussian and a non-Gaussian, for which we have developed an efficient algorithm to derive the solution. We have shown that we can also handle a non-diagonal covariance matrix. We have extended the method so it can deal with spherical maps, which is needed for future surveys such as the Euclid space mission. Our experiments clearly show a significant improvement compared to the state of art.

In the spirit of reproducible research, the MCA lens algorithm is publicly available in the CosmoStat's Github package<sup>3</sup>, including the material needed to reproduce the simulated experiences (folder examples/mcalens\_paper and script make\_fig.py).

## Acknowledgment

We thank Tim Schrabbaack for sending us his COSMOS shear catalog and the Columbia Lensing group (<http://columbialensing.org>) for making their suite of simulated maps available, and NSF for supporting the creation of those maps through grant AST-1210877 and XSEDE allocation AST-140041.

<sup>3</sup> <https://github.com/CosmoStat/cosmostat>



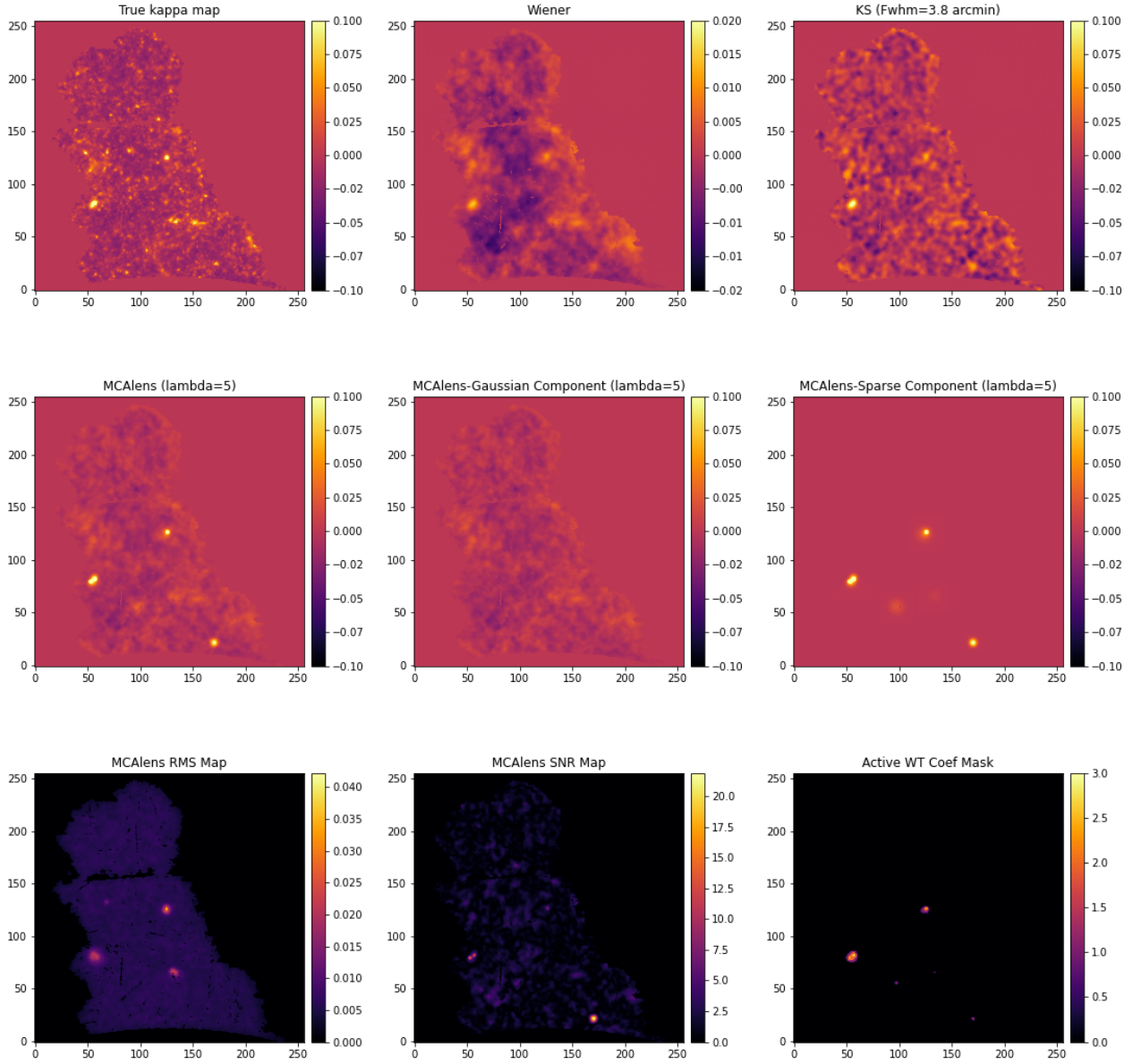


**Fig. 5.** Columbia convergence map recovery: Top, true convergence map, Wiener map, and Kaiser-Squires map smoothed with a Gaussian having a Full Width at Half Maximum of 3.8 arcmin. Middle, MCA lens map and its Gaussian and sparse and. The sum of these two last maps is equal to the first one. Bottom, RMS, SNR and significance maps.

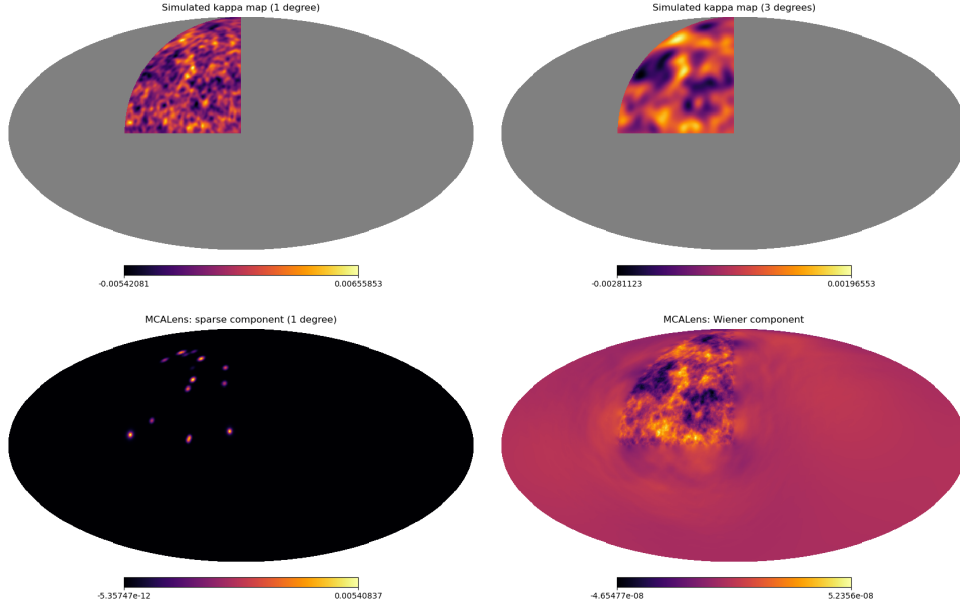


**Fig. 6.** MICE simulations: top, true convergence map at 1 and 3 degrees. Bottom, MCAIens sparse and Gaussian components.

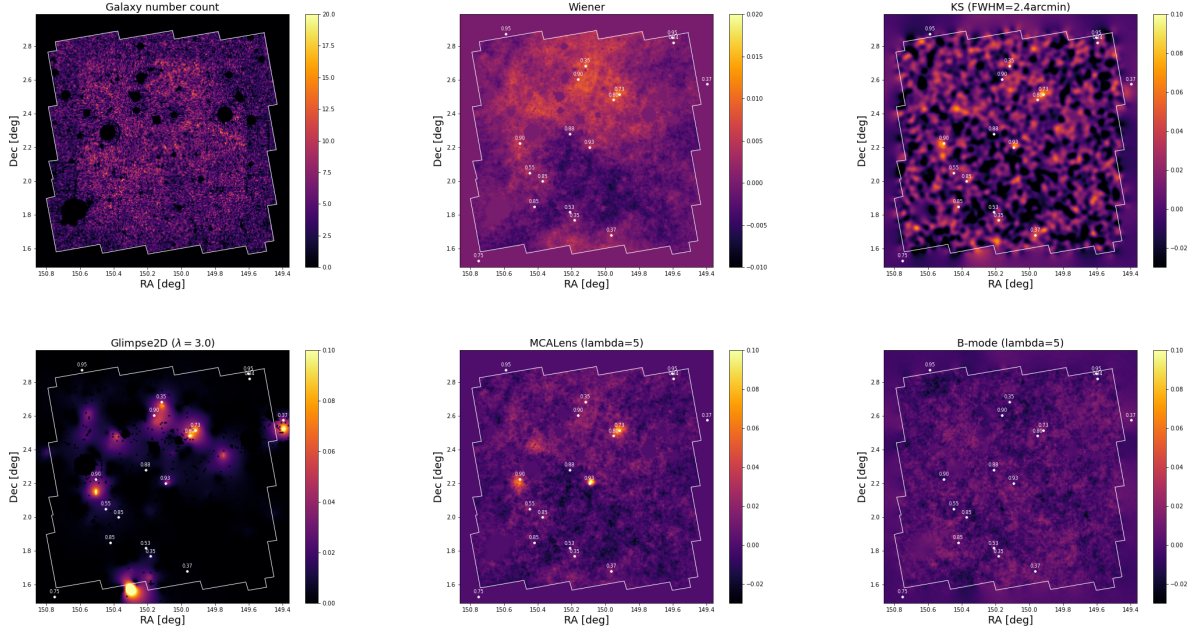


**Fig. 7.** COSMOS data: Top, galaxies count map, Wiener map, and Kaiser-Squires map smoothed with a Gaussian having a Full Width at Half Maximum of 2.4 arcmin. Bottom, Glimpse, MCAIens and MCAIens B-mode map.

## Appendix A: MICE simulations

We use the public MICE (v2) simulated galaxy catalogue, which is constructed from a lightcone N-body dark matter simulation (Fosalba et al. 2015; Crocce et al. 2015; Fosalba et al. 2015; Carretero et al. 2015; Hoffmann et al. 2015; Tallada et al. 2020). The MICE catalogue provides the calculated weak lensing (noise-free) observables: shear and convergence. In a given patch of simulated sky we select galaxies in the redshift<sup>4</sup>  $z$  range  $[0.6, 1.4]$ . Each galaxy corresponds to a noisy shear measurement, and we subsample with a density of  $\sim 8000$  galaxies per  $\text{deg}^2$ .

Uncorrelated, complex shape noise values are randomly drawn from a Gaussian distribution and added to the shear value of each selected galaxy. This noise per galaxy is zero mean and has variance  $2\sigma_\epsilon^2 = 0.1636$  (as estimated from data (Jeffrey et al. 2018a)). The final pixelised noise ( $\mathbf{n}$ ) has variance that depends on the number of galaxies per pixel.

In our simulated data, we mimic these conditions by choosing to remove all galaxies in given regions. Here there are no shear measurements available and the noise variance is effectively infinite.

The top row of Fig. A.1 shows a simulated convergence map with the DES SV footprint and mask, and the bottom row shows two simulated observed shear component maps,  $\gamma_1$  and  $\gamma_2$ .

## Appendix B: A Wiener tour

### Appendix B.1: Wiener and inpainting

Missing data is a common problem for galaxy surveys as foreground objects obscuring the background galaxies have to be “masked out”. In addition to the non stationary noise, observed shear fields therefore also present missing data. Noting the mask  $M$  as equal to 1 if we have shear measurements at a pixel position and zero otherwise, missing data can be handled in Wiener filtering by forcing the noise covariance matrix to be very high at locations where  $M = 0$ . This leads the solution to be different from zero and smoothed in the missing data area, and remove border effect artefacts. The Wiener filtering can therefore be seen as an inpainting technique, since it fills the missing area in the image. Alternative inpainting techniques were proposed in the past, through sparse recovery techniques (Pires et al. 2009; Lanusse et al. 2016) or Gaussian constraint realizations (Zaroubi et al. 1995; Jeffrey et al. 2018a). Since the Wiener model assumed the solution to be a Gaussian random field, it would make sense to have a solution where the inpainted area presents the same statistical properties as in non inpainted area. This property is by construction verified with constraint realizations, and it was shown it is also the case with sparse inpainting (Pires et al. 2009). A similar sparse inpainting can be very easily included in the proximal Wiener filtering, minimizing the following equation:

$$\kappa_G = \arg \min_{\kappa} \left\{ \|\mathbf{M}(\gamma - \mathbf{A}\kappa)\|_{\Sigma_n}^2 + \beta \|\kappa\|_{\Sigma_\kappa}^2 + \lambda \|\Phi^* \kappa\|_p \right\}, \quad (\text{B.1})$$

where  $p = 0$  or  $1$ ,  $\Phi$  is the Discrete Cosine Dictionary (DCT), and  $\lambda$  is a Lagrangian parameter. We end up with the forward-backward algorithm, called **InpWiener**:

– Forward step:

$$\mathbf{t} = \kappa^n + 2\mu \mathbf{A}^* \Sigma_n^{-1} (\mathbf{M}(\gamma - \mathbf{A}\kappa^n)) \quad (\text{B.2})$$

– Backward step:

$$\kappa^{n+1} = \mathbf{M}\mathbf{u} + (1 - \mathbf{M})\Delta_{\Phi, \lambda}\mathbf{u} \quad (\text{B.3})$$

where  $\Delta_{\Phi, \lambda}$  is the proximal operator defined in Pires et al. (2009) which consists in applying a DCT transform to  $\mathbf{u}$ , threshold the DCT coefficients and reconstruct an image from the thresholded coefficients, and

$$\mathbf{u} = \mathbf{F}^* \left( \mathbf{P}_\kappa (\mathbf{P}_\eta + \mathbf{P}_\kappa)^{-1} \right) \mathbf{F} \mathbf{t}, \quad (\text{B.4})$$

Areas where we have information are processed as in the usual Wiener case, while the inpainting regularization impacts area with missing data (i.e. when  $M = 0$ ).

Concerning Eq. B.1, it is interesting to note that:

<sup>4</sup> Redshift due to the expansion of the Universe is used as a proxy for distance to a galaxy, as it is an observable that monotonically increases with distance from an observer.

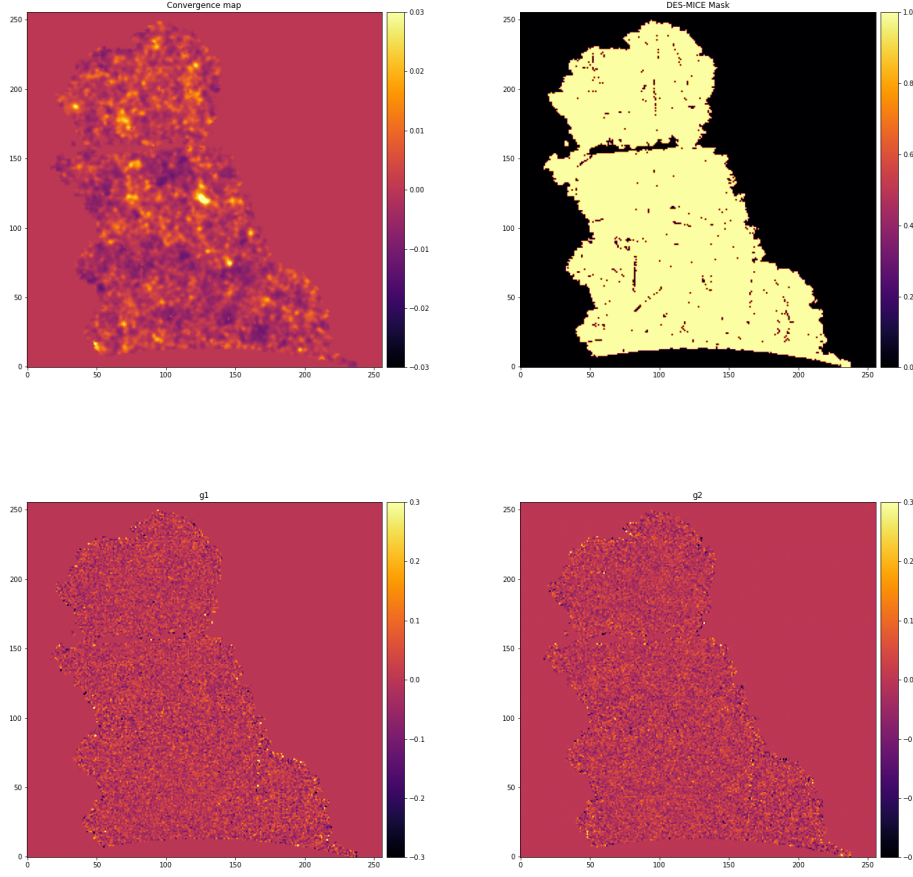


**Fig. A.1.** Top, true MICE convergence map with DES SV footprint and mask. Bottom, Two simulated observed shear components,  $\gamma_1$  and  $\gamma_2$ .

- **KS**: if  $\beta = 0, \lambda = 0$  and  $\Sigma_n$  is diagonal with constant values along the diagonal (i.e. stationary Gaussian noise), **InpWiener** leads to the non-iterative standard Kaiser-Squires solution.
- **GKS**: If  $\beta = 0$  and  $\lambda = 0$ , the least square estimator is derived with the iterative algorithm:  $\kappa^{n+1} = \kappa^n + 2\mu \mathbf{A}^* \Sigma_n^{-1} (M(\gamma - \mathbf{A} \kappa^n))$ , with  $\mu = \min(\Sigma_n)$ . As it generalizes the Kaiser-Squires method, we will call this algorithm **GKS**.
- **FASTLens**: If  $\beta = 0$  and  $\Sigma_n$  is diagonal with constant values along the diagonal, **InpWiener** leads to the FASTLens inpainting algorithm (Pires et al. 2009).
- **GIKS**: If  $\beta = 0$ , **InpWiener** leads to an inpainted generalized the Kaiser-Squires solution where the **InpWiener** Forward is unchanged, and the Backward step becomes:

$$\kappa^{n+1} = M t + (1 - M) \Delta_{\Phi, \lambda} t \quad (\text{B.5})$$

Similarly to sections 3.5 and 3.5, these algorithms can handle data on the sphere and reconstruct jointly E and B modes.

#### Inpainted Wiener Experiment

To test **InpWiener**, we use the public MICE (v2) simulated galaxy catalogue presented Appendix A.

Figure B.1 shows the Wiener solution (left) and the inpainted Wiener solution (right) derived from the shear components shown in Fig. A.1.

#### Appendix B.2: Agnostic Wiener Filtering

The Wiener method needs to know the theoretical power spectrum  $P_\kappa$ , and the solution therefore varies with the assumed cosmological model used to derive  $P_\kappa$ . To avoid this issue, a solution could be to estimate  $P_\kappa$  directly from the shear measurements, for instance using a mask correction as in Upham et al. (2020). Bayesian techniques have also been used to infer both the map and power spectrum (Wandelt et al. 2004; Jasche & Lavaux 2014; Alsing et al. 2016a). An alternative approach is to use the **GIKS** inpainting algorithm to fill first the missing area and then to compute the power spectrum of the inpainted map. Applying **GIKS** on the data and a set of  $R$  noise realizations, the final estimator is

$$P_\kappa = \text{powspec}(\kappa_{\text{Data}}) - \frac{1}{R} \sum_i \text{powspec}(\kappa_{\text{Rea}_i}). \quad (\text{B.6})$$

Since the data noise  $P_\kappa$  will still be noisy, a final denoising step or a function fitting can be done.

As an illustration, we fitted the function  $f(k, a, u, e, c) = \exp(|a * (uk)^{-e}|) + c$  to the estimated noisy  $P_\kappa$ . Figure B.2 shows an example of an estimated power spectrum following this approach.

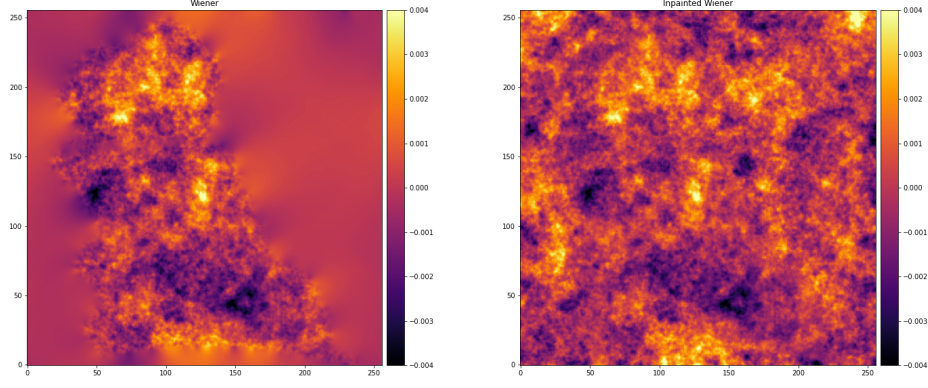


**Fig. B.1.** Wiener and inpainted Wiener solutions.

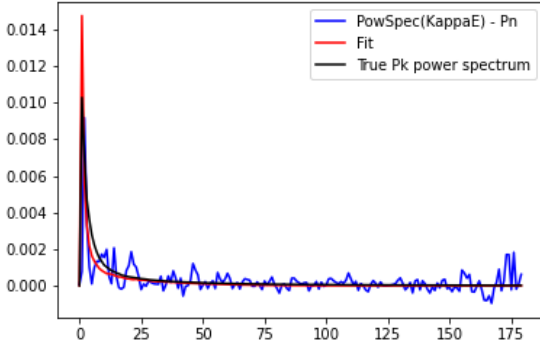


**Fig. B.2.** Theoretical power spectrum of one convergence map. In black the true theoretical power spectrum; in red, the spectrum estimated using the **GIKS** algorithm, corrected from noise power spectrum, and in blue the fit.

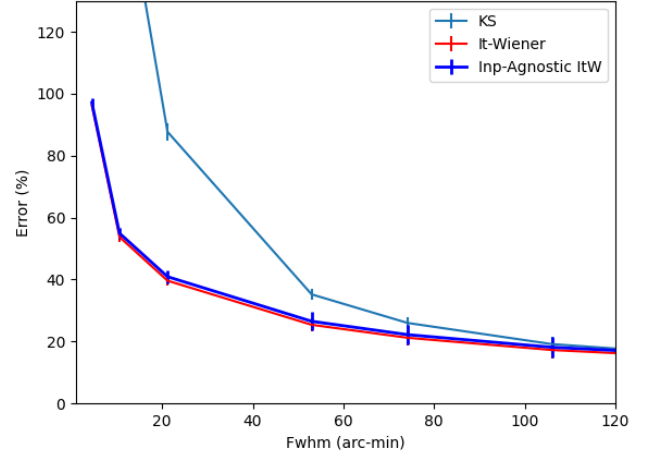


**Fig. B.3.** Reconstruction error at different resolution for Kaiser-Squires, Wiener and inpainted agnostic Wiener.

## Experiment: Impact of an unknown theoretical power spectrum

In this experiment, we used the same public MICE simulations, and we extracted 18 shear different shear maps with different noise realizations. For each of them, we applied the forward-backward Wiener algorithm using the true theoretical power spectrum, and we applied the inpainted agnostic Wiener method on the same data, re-estimating for each of the 18 shear data sets the theoretical power spectrum. Fig. B.3 shows the reconstruction errors at different resolutions, for Kaiser-Squires, Wiener and inpainted agnostic Wiener. We can easily see that the inpainting has no impact on the reconstruction error, which is expected since only the area where the mask is equal to one is used in the error calculation, and also that the agnostic approach also has very little impact on the final solution. We do not claim that we should use an agnostic approach when applying a Wiener filtering, but it is interesting to have this option available, i.e. when using Wiener without any assumption about the cosmology, and to give us the possibility to check if cosmological priors impact the results.

## References

- Abell, P. A., Burke, D. L., Hamuy, M., et al. 2009, *Lsst science book*, version 2.0, Tech. rep.
- Ajani, V., Peel, A., Pettorino, V., et al. 2020, arXiv e-prints, arXiv:2001.10993
- Alsing, J., Heavens, A., & Jaffe, A. H. 2016a, *Monthly Notices of the Royal Astronomical Society*, 466, 3272
- Alsing, J., Heavens, A., & Jaffe, A. H. 2017, *MNRAS*, 466, 3272
- Alsing, J., Heavens, A., Jaffe, A. H., et al. 2016b, *MNRAS*, 455, 4452
- André, P., Men'shchikov, A., Bontemps, S., et al. 2010, *A&A*, 518, L102
- Bartelmann, M. & Schneider, P. 2001, *Physics Reports*, 340, 291
- Bobin, J., Starck, J. L., Sureau, F., & Fadili, J. 2012, *Advances in Astronomy*, 2012, 703217
- Bobin, J., Sureau, F., & Starck, J. L. 2016, *A&A*, 591, A50
- Carretero, J., Castander, F. J., Gaztañaga, E., Crocce, M., & Fosalba, P. 2015, *MNRAS*, 447, 646
- Chang, C., Pujol, A., Mawdsley, B., et al. 2018, *MNRAS*, 475, 3165
- Combettes, P. L. & Wajs, V. R. 2005, *Multiscale Modeling & Simulation*, 4, 1168
- Crocce, M., Castander, F. J., Gaztanaga, E., Fosalba, P., & Carretero, J. 2015, *MNRAS*, 453, 1513
- Elad, M., Starck, J.-L., Donoho, D., & Querre, P. 2005, *Applied and Computational Harmonic Analysis*, 19, 340–358
- Elsner, F. & Wandelt, B. D. 2013, *A&A*, 549, A111
- Finoguenov, A., Guzzo, L., Hasinger, G., et al. 2007, *ApJS*, 172, 182
- Fluri, J., Kacprzak, T., Sgier, R., Refregier, A., & Amara, A. 2018, *J. Cosmology Astropart. Phys.*, 2018, 051
- Fosalba, P., Crocce, M., Gaztanaga, E., & Castander, F. J. 2015, *MNRAS*, 448, 2987

- Fosalba, P., Gaztanaga, E., Castander, F. J., & Crocce, M. 2015, MNRAS, 447, 1319
- Górski, K. M., Hivon, E., Banday, A. J., et al. 2005, Astrophysical Journal, 622 [arXiv:astro-ph/0409513], 759–771
- Hoffmann, K., Bel, J., Gaztanaga, E., et al. 2015, MNRAS, 447, 1724
- Horowitz, B., Seljak, U., & Aslanyan, G. 2019, J. Cosmology Astropart. Phys., 2019, 035
- Jain, B. & Van Waerbeke, L. 2000, ApJ, 530, L1
- Jasche, J. & Lavaux, G. 2014, Monthly Notices of the Royal Astronomical Society, 447, 1204
- Jeffrey, N., Abdalla, F. B., Lahav, O., et al. 2018a, MNRAS, 479, 2871
- Jeffrey, N., Heavens, A. F., & Fortio, P. D. 2018b, Astronomy and Computing, 25, 230
- Jeffrey, N., Lanusse, F., Lahav, O., & Starck, J.-L. 2020, MNRAS, 492, 5023
- Joseph, R., Courbin, F., Starck, J. L., & Birrer, S. 2019, A&A, 623, A14
- Kaiser, N. & Squires, G. 1993, ApJ, 404, 441–450
- Kilbinger, M. 2015, Reports on Progress in Physics, 78, 086901
- Kilbinger, M., Fu, L., Heymans, C., et al. 2013, MNRAS, 430, 2200
- Kratochvil, J. M., Lim, E. A., Wang, S., et al. 2012, Phys. Rev. D, 85, 103513
- Lanusse, F., Starck, J.-L., Leonard, A., & Pires, S. 2016, A&A, 591, A2
- Laureijs, R., Amiaux, J., Arduini, S., et al. 2011, arXiv preprint arXiv:1110.3193
- Leonard, A., Dupé, F.-X., & Starck, J.-L. 2012, A&A, 539, A85
- Li, Z., Liu, J., Matilla, J. M. Z., & Coulton, W. R. 2019, Phys. Rev. D, 99, 063527
- Lin, C.-A. & Kilbinger, M. 2015, A&A, 576, A24
- Liu, J., Bird, S., Matilla, J. M. Z., et al. 2018, J. Cosmology Astropart. Phys., 2018, 049
- Liu, J. & Haiman, Z. 2016, Phys. Rev. D, 94, 043533
- Marian, L., Hilbert, S., Smith, R. E., Schneider, P., & Desjacques, V. 2011, ApJ, 728, L13
- Mawdsley, B., Bacon, D., Chang, C., et al. 2020, MNRAS, 493, 5662
- Melchior, P., Moolekamp, F., Jerdee, M., et al. 2018, Astronomy and Computing, 24, 129
- Möller, A., Ruhlmann-Kleider, V., Lanusse, F., et al. 2015, J. Cosmology Astropart. Phys., 2015, 041
- Munshi, D. & Coles, P. 2017, Journal of Cosmology and Astroparticle Physics, 2017, 010
- Peel, A., Lanusse, F., & Starck, J.-L. 2017a, The Astrophysical Journal, 847, 23
- Peel, A., Lin, C.-A., Lanusse, F., et al. 2017b, A&A, 599, A79
- Petri, A., Haiman, Z., Hui, L., May, M., & Kratochvil, J. M. 2013, Phys. Rev. D, 88, 123002
- Pires, S., Starck, J. L., Amara, A., et al. 2009, MNRAS, 395, 1265
- Price, M. A., Cai, X., McEwen, J. D., et al. 2020a, MNRAS, 492, 394
- Price, M. A., McEwen, J. D., Cai, X., Kitching, T. D., & LSST Dark Energy Science Collaboration. 2019, MNRAS, 489, 3236
- Price, M. A., McEwen, J. D., Pratley, L., & Kitching, T. D. 2020b, arXiv e-prints, arXiv:2004.07855
- Repetti, A., Pereyra, M., & Wiaux, Y. 2019, SIAM Journal on Imaging Sciences, 12, 87
- Schrabback, T., Hartlap, J., Joachimi, B., et al. 2010, A&A, 516, A63
- Scoville, N., Abraham, R. G., Aussel, H., et al. 2007, ApJS, 172, 38
- Shirasaki, M., Yoshida, N., Hamana, T., & Nishimichi, T. 2012, ApJ, 760, 45
- Spergel, D., Gehrels, N., Baltay, C., et al. 2015, arXiv preprint arXiv:1503.03757
- Starck, J.-L., Candès, E., & Donoho, D. 2003, A&A, 398, 785–800
- Starck, J.-L., Elad, M., & Donoho, D. 2004, Advances in Imaging and Electron Physics, 132
- Starck, J.-L., Moudén, Y., Abrial, P., & Nguyen, M. 2006, A&A, 446, 1191–1204
- Starck, J.-L., Murtagh, F., & Fadili, J. 2015, Sparse Image and Signal Processing: Wavelets and Related Geometric Multiscale Analysis (Cambridge University Press)
- Starck, J.-L., Pires, S., & Réfrégier, A. 2006, A&A, 451 [astro-ph/0503373], 1139–1150
- Tallada, P., Carretero, J., Casals, J., et al. 2020, Astronomy and Computing, 32, 100391
- Teyssier, R. 2002, A&A, 385 [astro-ph/0111367], 337–364
- Upham, R. E., Whittaker, L., & Brown, M. L. 2020, MNRAS, 491, 3165
- Wagner-Carena, S., Hopkins, M., Diaz Rivero, A., & Dvorkin, C. 2020, MNRAS, 494, 1507
- Wandelt, B. D., Larson, D. L., & Lakshminarayanan, A. 2004, Phys. Rev. D, 70, 083511
- Wiener, N. 1949, Extrapolation, interpolation, and smoothing of stationary time series: with engineering applications, Vol. 7 (MIT press Cambridge)
- Zaroubi, S., Hoffman, Y., Fisher, K. B., & Lahav, O. 1995, Astrophysical Journal, 449, 446